

Nano- and Micro-structuring of Materials Using Polymer Cold Drawing Process



Ming Chen, Zhixun Wang, and Ke He

Abstract Cold drawing is a well-established manufacturing process for tailoring properties of polymers in polymer industries. It refers to the phenomenon that necks formed during the tensile drawing of polymer fibers, films, or any other shapes. The necking reduces the height and width of the polymer sample being stretched and elongates it in length. The cross-sectional area in the necking region becomes smaller and keeps in a constant value with traveling to the remaining non-necking regions until the non-necking regions disappeared. Fundamentally, cold drawing is the movements and orientations of entangled polymer chains under external forces. It happens both for amorphous and for semicrystalline polymers in specific conditions. Though the cold drawing process has long been used in industrial applications, it has been rediscovered as a method of nano- and micro-structuring of materials recently. Materials used for structuring are wrapped in polymer fiber to form a core-shell structure or attached to the surface of the polymer substrate, then experience ordered fragmentations during the cold drawing of the composite structure, and finally formed regular patterns in nano- and micro-scale. This robust nano- and micro-structuring process is easy to perform and can be conducted using bare hands in some situations. Further, this method can be applied to various materials and is suitable for large-scale fabrication. This chapter discusses nano- and micro-structuring of materials including crystal, glass, and polymer with the core-shell structured fiber and film-based flat geometries.

Ming Chen and Zhixun Wang—Equally contributed.

M. Chen (✉) · K. He

Center for Information Photonics and Energy Materials, Shenzhen Institutes of Advanced Technology, Chinese Academy of Sciences, Shenzhen 518055, People's Republic of China
e-mail: ming.chen2@siat.ac.cn

Z. Wang

School of Electrical and Electronic Engineering, Nanyang Technological University, 50 Nanyang Avenue, Singapore 639798, Singapore

K. He

Department of Nano Science and Technology Institute, University of Science and Technology of China, Suzhou 215123, People's Republic of China

Keywords Cold drawing · Nano- and micro-structuring · Controlled fragmentations · Shear-lag theory · Metal film · Two-dimensional materials · Micro-ribbons

1 Introduction

In the polymer industries, cold drawing is a successful technique used in the production of polymer with enhanced mechanical properties, such as high tensile strength polyester and nylon fibers (Carragher 2017; Ziabicki 1976). First discovered in the 1940s (Carothers and Hill 1932), cold drawing refers to the phenomenon that many polymers, when subjected to tensile stress, may undergo non-homogeneous deformation with one or multiple necking regions formed after the initial small homogeneous elastic deformation. The movements of polymer chains are the underlying mechanism of this phenomenon. The ‘frozen’ polymer chains can move under the external tensile force. The nature of this mechanical instability is high-elastic state deformation or forced high-elastic state deformation since the deformation only recovers when the specimen being annealed at around the glass transition temperature (for amorphous polymers) or the melting temperature (for semicrystalline polymers). The interesting part of this non-homogeneous deformation is, clear boundaries or necking fronts, lying normal to the drawing direction can be observed between the necking and non-necking regions. The necking regions elongated in the drawing direction and shrank in the dimension perpendicular to the drawing direction. With the cold drawing process goes on, the necking regions extend by the traveling of necking fronts until the non-necking regions disappeared. In the propagation of necking fronts, strong strain localized only in the necking fronts, while the necking and non-necking regions are stable. Eventually, the specimen becomes stronger after the necking fronts went through it, which is called strain hardening (Vincent 1960; Coleman 1985). While the forming of neck fronts is influenced by many factors, such as the drawing temperature, the drawing rate, and the molecular weight, many polymers can be cold drawn under ambient temperature.

The studies on cold drawing focused on single material in the past decades (Argon 2013), cold drawing of a composite structure emerged later which concentrated on fiber reinforcement composites (Loos et al. 2001; Friedrich et al. 2005; Fakirov et al. 2007). Yet until recently, research works on using cold drawing to form nano- and micro-structures have been reported (Shabahang et al. 2016; Xu et al. 2017; Wu et al. 2019; Loke et al. 2019; Chen et al. 2017, 2019; Wang et al. 2010; Nairn 1997; Galiotis and Paipetis 1998; Li et al. 2018). There are two geometries have been investigated, namely the core-shell structured fiber and planar film-based composite. The designed core-shell structured fibers are consisting of a ductile polymer shell and a core of another relatively brittle material. The polymer shell experiences cold drawing under tensile stretching; consequently, the core material be affected through the stress transferred through the interfaces. When the stress in the core material exceeds the tensile strength of it, the core material breaks. Rather than random fragmentations, a

sequentially ordered break-up of the core material happens and results in a periodic chain of rods separated by voids. The strong localized strain in the necking fronts leads to the controllable fragmentations. Core material only breaks after the necking fronts propagated through, and other parts located in the non-necking regions remain intact. The size of fragments depends on the diameter and Young's modulus of the core material. From this method, various multicomponents nano- and micro-structures can be produced on a large scale. In addition, the uniformly sized rods of the core material can be etched out via the selective dissolution of the polymer shell. In principle, any material which does not undergoes cold drawing can be used as the core material, including crystals, glasses, and polymers. For the planar film-based composite, a similar phenomenon can be observed. A thin layer of relatively brittle material, for example, glass or metal can be deposited on a polymer film, which can be cold drawn. After the process of cold drawing, the thin deposited layer fragments in the transverse direction sequentially and resulting in ordered ribbons array. The formed pattern has a featured size of nanometers to microns. Further, submicron ribbons of monolayer or few layers two-dimensional transition metal dichalcogenides (TMDs) and graphene can be produced by this lithography-free approach. This versatile method can be applied to other low-dimensional materials.

To understand the underlying mechanism of the ordered fragmentations, the shear-lag theory was modified to explain this phenomenon. The traditional shear-lag theory was first reported in the 1940s and well-established for the mechanical analysis of composites, especially for fiber-reinforced composites (Wang et al. 2010; Nairn 1997; Galiotis and Paipetis 1998). In the traditional shear-lag model, the strain is distributed globally in contrast to the cold drawing process where the strain is localized in the necking fronts. Also, the traditional shear-lag fragmentations typically occur at random locations simultaneously, while the target material only fragments with the necking front passing through in the cold drawing process. Besides, the traditional shear-lag model and the cold drawing process share the same interfacial stress transfer mechanism. A modified shear-lag model can be applied in the analysis of the cold drawing process.

2 Cold Drawing of Core-Shell Structured Fibers

A wire-like core material embedded in a polymer fiber matrix assembles a core-shell structured fiber composite. The core-shell structured fiber provides a good platform to study the cold drawing on composite in which the shell undergoes cold drawing and the core does not. The mismatch in mechanical properties for the core and the shell materials leads to different mechanical behaviors for them during the cold drawing process.

2.1 Fabrication of Core-Shell Structured Fibers

The 1-mm-diameter fibers used for cold drawing have a shell of thermoplastic polymer polyethersulfone (PES). It is chosen to be used as the shell material because it undergoes cold drawing at ambient temperature, using other polymers (which undergo cold drawing) can get similar results. To demonstrate the universality of this method, a wide range of materials is used as core material, including four glasses: silica (SiO_2), tellurite glass $70\text{TeO}_2-20\text{ZnO}-5\text{K}_2\text{O}-5\text{Na}_2\text{O}$ (TeG), phosphate glass (PeG), and chalcogenide glasses As_2Se_3 (ChG); five polymers: polystyrene (PS), acrylonitrile butadiene styrene (ABS), polyethylene oxide (PEO), silk, and human hair; and three crystals: silicon (Si), germanium (Ge), and ice. The fibers consisting of a 20- μm -diameter core of ChG are fabricated via fiber thermal drawing technique (PES and ChG are thermally compatible), which is a scale-down process of a macroscopic scale perform, and the process is diagrammed in Fig. 1a. The same technique is applied for thermally compatible core materials. For other core materials which are thermally incompatible with PES, they are placed into hollow PES fibers (prepared from thermal drawing) and annealed to ensure the strong adhesion between the shell and the core (Fig. 1b). The fibers with ice core are fabricated by first filling water into hollow PES fibers and then frozen at -5°C .

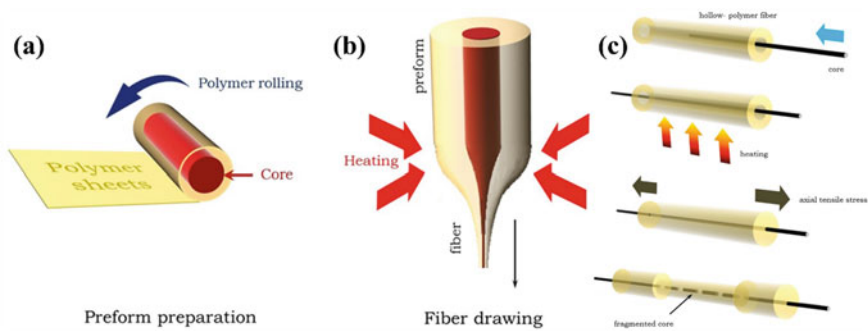


Fig. 1 Schematic illustration for the fabrication of core-shell structured fibers. **a** Schematic depiction of the thin-film-rolling process. A cylindrical rod of a material to be used as a core is rolled with thin PES sheets and then thermally consolidated under vacuum to fuse the thin films and yield a preform. **b** The preform is heated in a custom-built fiber draw tower, and axial tension is applied to elongate the preform into a fiber (along the direction of the arrow). **c** Schematic depiction of combining a thermally incompatible micro-wire and a hollow polymer fiber for cold drawing. Adapted with permission from Shabahang et al. (2016)

2.2 Ordered Fragmentation of the Core Material

The core-shell-structured fibers are subjected to cold drawing after preparation. The cold drawing is conducted by fixing the ends of the specimen on a travel stage; then, the travel stage stretches the specimen at a constant speed. Interestingly, this simple process can be also done using bare hands, as shown in Fig. 2a.

All the tested core materials fragmented into ordered rods after the cold drawing. For the characterization of the fragmentation process, optical images are taken for the different stages of the cold drawing process for the PES-cladding and ChG-core fiber. Figure 2e is the optical image taken before the neck forms, the initial stage of necking, and the propagation of the necking front, respectively. The core ChG is observed to fragment into ordered micro-rods after the cold drawing process. The enlarged image in Fig. 2f shows the details of the fragmentation. The core in neck regions has fractured into rods, while other parts located in non-necking regions remain intact. It can be seen clearly that the fragmentation of core material happens in the necking front. The extracted ChG rods shown in Fig. 2j demonstrate the potential of this method as a mass fabrication tool for micro-rods. Figure 2i illustrates the whole process. It is worth noting that this method is not limited by fiber geometries, and as shown in Fig. 2b–d, cylindrical, rectangular, and triangular fibers can be cold drawn in spite of their difference in the shape of cross section.

Some results can be found with a systematic investigation of the obtained rods. In Fig. 3a, a linearly proportional relationship between the average length L and the diameter D of the rods can be clearly observed both for ChG and TeG. The linear proportionality $f = L/D$ depends on the core material. Figure 3b plots the relationship between f and the Young's modulus of eleven different core materials. It can be found empirically that $f \propto \sqrt{E}$, where E is the Young's modulus of the core material. Considering the similarity in geometries between the core-shell structured fibers and fiber-reinforced composites, the interfacial mechanical behaviors of the core-shell structured fibers could possibly follow the classic shear-lag theory. Verified with experiments, the modified shear-lag model $\bar{L}/D = \sqrt{E/\Omega}$ (Galiotis and Paipetis 1998; Thostenson et al. 2002; Kim and Nairn 2002; Figueroa et al. 1991), where Ω is a characteristic stress (equals to 0.1 GPa as shown in Fig. 3c), is in a good agreement with experimental results (Table 1).

3 Cold Drawing of Film-Based Flat Composites

Apart from the core-shell fiber structures, cold drawing of film-based flat composites can lead to interesting results as well. There are mainly two types of film-based flat composites studied, one is the two-layer structure, and the other one is the polymer film/core film/polymer film sandwiched structure (Xu et al. 2017; Wu et al. 2019; Chen et al. 2017, 2019). The interfacial mechanical behaviors between core film

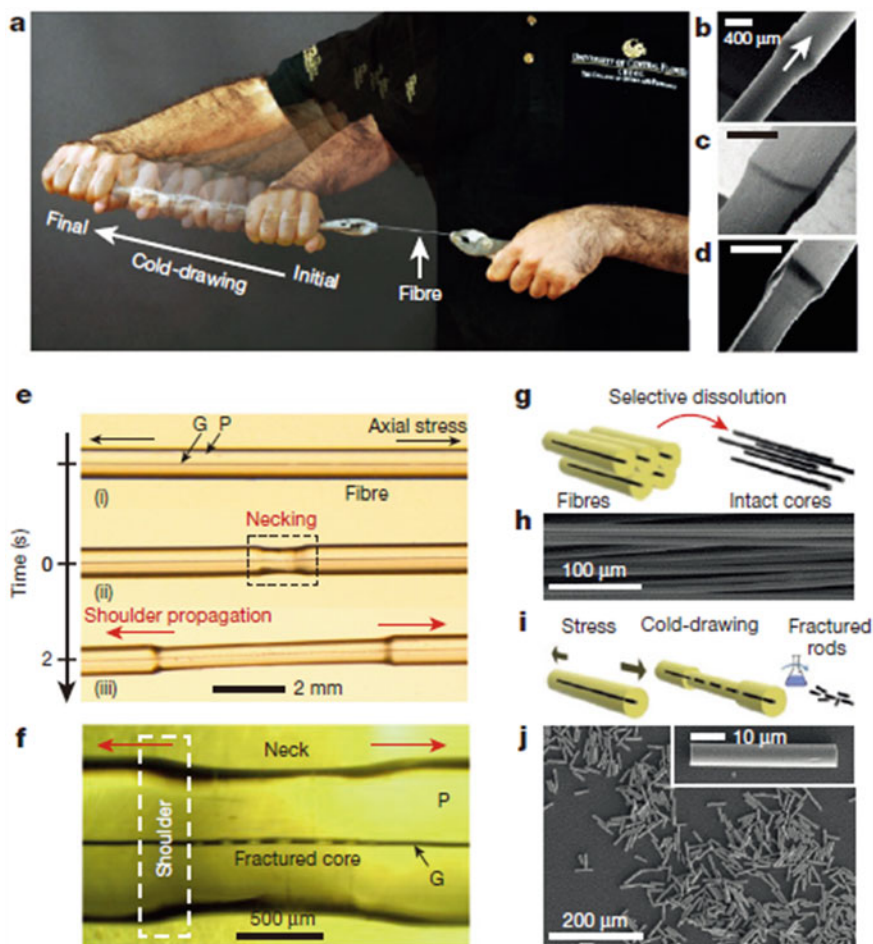


Fig. 2 Fragmentation *via* a cold drawing-induced, propagating, mechanical–geometric instability. **a** Photograph of a polymer fiber undergoing cold drawing under axial stress at a speed of approximately 5 mm s^{-1} . Multiple shots taken over 1 min are overlaid to highlight the extent of fiber elongation. **b–d** Scanning electron microscope (SEM) micro-graphs of the propagating shoulder in polymer (PES) fibers with cross sections that are circular (diameter of 0.7 mm); **(b)**, rectangular (side lengths of 0.2 and 1 mm); **(c)** and equilaterally triangular (side length of 0.4 mm); **(d)**. Scale bars, $400 \mu\text{m}$. **e** Transmission optical micro-graphs of a multimaterial cylindrical fiber undergoing cold drawing at 3 mm s^{-1} captured at three different stages: **(i)** initially intact fiber; **(ii)** neck formation; and **(iii)** shoulder propagation, leaving behind a fractured core after fragmentation. The cladding is a polymer ‘P’ (PES), and the core is a glass ‘G’ (As_2Se_3). **f** A magnified transmission micro-graph of the neck region, corresponding to the dashed black rectangle in **e**. The dashed white rectangle highlights the propagating instability, wherein fragmentation takes place. **g** Schematic of selective dissolution of the polymer cladding to retrieve intact cores. **h** SEM micro-graph of retrieved intact glass cores from multiple fibers. **i, j** Schematic **(i)** and SEM micro-graph **(j)** of retrieved nano-fragmented micro-rods by selective dissolution from a cold-drawn fiber. Inset in **j** is an SEM micro-graph of a single micro-rod. Adapted with permission from Shabahang et al. (2016)

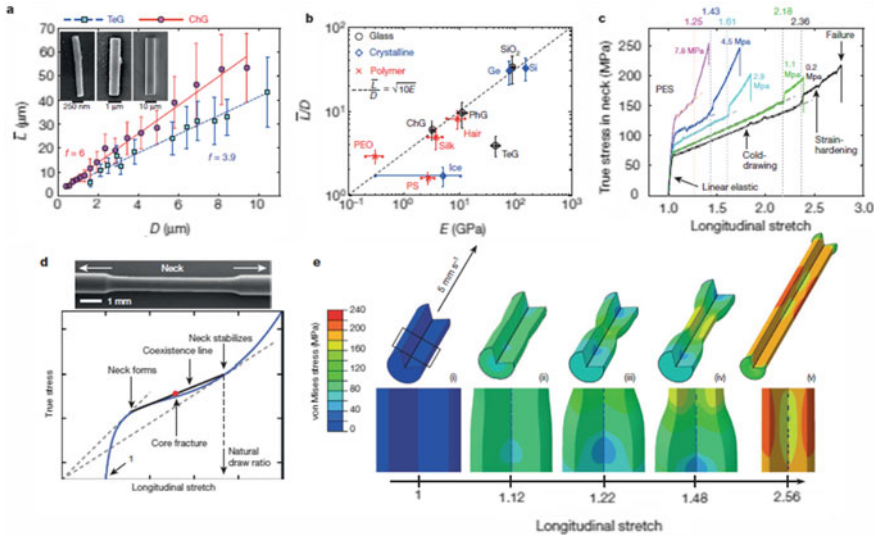


Fig. 3 Characterization of fragmentation induced by cold drawing of a PES fiber. **a** Measurements of the average length \bar{L} of fragmented micro- and nano-rods of chalcogenide glass (ChG; As_2Se_2 ; red circles) and tellurite glass (TeG; $70TeO_2-20ZnO-5K_2O-5Na_2O$; blue squares) of diameter D in a PES fiber upon cold drawing. The red solid and blue dashed lines are linear fits with slopes $f = \bar{L}/D = 6$ and 3.9 for ChG and TeG, respectively. Vertical error bars represent the root-mean-squared (r.m.s.) length dispersion of rods at each value of D . Insets are SEM micro-graphs of individual rods resulting from the cold drawing-driven fragmentation of As_2Se_3 cores of diameters (from left to right) 200 nm , $1\text{ }\mu\text{m}$, and $10\text{ }\mu\text{m}$. **b** Measured values of f for a host of materials embedded in a PES fiber plotted against their Young’s modulus E ; the dashed line corresponds to the ansatz $f \approx \sqrt{E/\Omega}$, with $\Omega = 0.1\text{ GPa}$ (such that $f \approx \sqrt{10E}$ when E is in gigapascals). Vertical error bars represent the measured r.m.s. dispersion in f ; horizontal error bars correspond to the uncertainty in the measured E (those for TeG and ice reflect the range of reported values). PhG, phosphate glass; PEO, polyethylene oxide; PS, polystyrene. **c** Stress–strain measurements of cylindrical PES fibers produced by thermal drawing at different prestress values (ranging from 0.2 to 7.8 MPa ; see colored-coded labels) identifying the four stages of linear elasticity, cold drawing, strain-hardening, and failure. The coexistence (dashed) lines and natural draw ratios (vertical dotted lines; values given above the plot) at neck stabilization (both defined in **d**) are identified. **d** Schematic representation of Considère model. The blue curve corresponds to the true stress versus stretch in a strain-controlled experiment. The solid black ‘coexistence’ line indicates necked and unnecked regions coexisting at equal engineering stresses as local stretch varies from the onset of necking to the natural draw ratio at which stable neck propagation occurs. The dashed black lines serve as guides to the eye. Above the plot is an SEM micro-graph of a necked region in a PES fiber; the arrows indicate the direction of the axial stress and shoulder propagation. **e** Von Mises stress distributions from finite-element simulations of in-fiber core (As_2Se_3) fragmentation during cold drawing of a PES fiber. The five steps (i–v) correspond to increasing stretch values. Top panels depict the full fiber; bottoms panels show the regions corresponding to that highlighted by the rectangle in (i). Adapted with permission from Shabahang et al. (2016)

Table 1 Measured values of \bar{L}/D and measured and reported values of E , for different core materials

Material	\bar{L}/D	St. Dev.	E (GPa)	Δ (GPa)	E (GPa)	Δ (GPa)
	Measured		Measured		Reported	
SiO ₂	33	11.95	88.5	5.5	70	65–73.1
Si	32.5	9.56	152	7.5	150	130–202
Ge	30	9.26	78	6	103	102.7–103
PhG ^{42–44}	9.5	3.19	11	2	55	31.3–79
Silk ^{45–47}	8.2	2.07	9	3.2	16	3.8–17
ChG ^{48–50}	6	1.57	3.2	0.1	38.6	18–40
TeG ⁵¹	3.9	1.07	N/A ⁽¹⁾	N/A ⁽¹⁾	44	37.1–50.7
Hair ^{52,53}	4.9	1.46	3.7	1.1	4	2.5–7.5
PEO ^{54,55}	2.9	0.56	0.3	0.1	5	0.2–7
Ice ^{20,44,56}	1.7	0.46	N/A ⁽²⁾	N/A ⁽²⁾	5.1	0.3–10
PS	1.6	0.25	2.7	0.7	3.2	3–3.5

Adapted with permission from Shabahang et al. (2016)

and polymer film follow the shear-lag theory for both types. For the core material, metals like silver (Ag), gold (Au), aluminum (Al), copper (Cu), platinum (Pt), and nickel (Ni) have been used, and the resulted nano-structures find a great potential in the applications of surface-enhanced Raman scattering (SERS) sensing (Wu et al. 2019), optical superlenses (Li et al. 2018), and localized surface plasmon resonance (LSPR) sensing (Xu et al. 2017). Further, two-dimensional materials, monolayer and few-layer transition metal dichalcogenides (TMDs), and graphene are used as core film both for investigating the mechanical behaviors of two-dimensional materials/polymer composites and fabricating two-dimensional materials submicron ribbons (Chen et al. 2017, 2019). This method is demonstrated as a versatile approach for large-scale two-dimensional material ribbons array production, and the fabricated ribbons array has a wide range of applications in nano-electronics.

3.1 Metal-Polymer Composites

A thin layer of metal elements can be deposited onto a polymer film via e-beam technique. A thin layer (~25 nm) of Ag was deposited onto a 20- μ m-thick poly(ϵ -caprolactone) (PCL) film before conducting the cold drawing process at a stretching speed of ~5 mm/s, as shown in Fig. 4.

After cold drawing, the Ag layer on PCL film has fragmented into ordered ribbons perpendicular to the drawing direction. And uniformly submicron wrinkles can be observed on the whole length of the ribbons, which is lying in the direction of drawing.

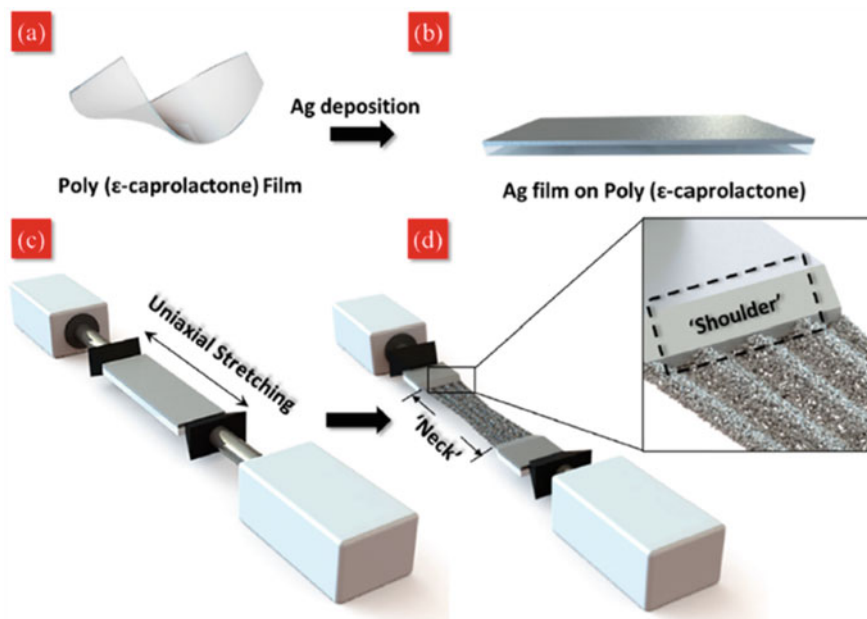


Fig. 4 Schematic diagram of stretching polymer SPR film under an external mechanic force. **a** Flexible PCL polymer film. **b** Ag film is deposited on PCL polymer film by an electron beam evaporator. **c** The polymer SPR film is fixed onto a mechanical machine. **d** The uniaxial stretching of polymer SPR film at a constant stretching speed. Two primary characteristics are observed: neck formation and shoulder propagation. The inset highlights the nano-structures' formation in the neck region. Adapted with permission from Xu et al. (2017), copyright (2020) American Chemical Society

The scanning electron microscope (SEM) images of the PCL film (without Ag layer deposited on) and Ag/PCL film after cold drawing are demonstrated in Fig. 5a, b.

While the ribbons have a feature size of tens of micrometers, the nano-grooves are observed to have a width of a hundred of nanometers between each wrinkle, shown in Fig. 5c. On each Ag wrinkle, there are uniformly distributed nano-gaps with a size of tens of nanometers on the surface. The atomic force microscope (AFM) was used to verify the surface morphology of resulted Ag ribbons with wrinkles, as illustrated in Fig. 5d. From the AFM images, the wrinkles are found to have a height of ~ 100 nm and a width of ~ 1 μm . To shed a light on the formation of wrinkles on the ribbon surface, a PCL film without Ag layer deposited on has been cold drawn (Fig. 5a), as can be seen that many wrinkles formed on the surface of PCL film, considering the nature of semicrystalline polymer for PCL film, Poisson's ratio (~ 0.45) of PCL, and the relatively fast drawing rate, the formation of wrinkled surface can be attributed to the deformation of PCL film. During the cold drawing process, the PCL crystals reoriented and further shrank laterally, and the distance between each adjacent lamellae increased within a crystal. For PCL film with Ag layer deposited on, the Ag particles act as blocks preventing the wrinkles from overlapping and

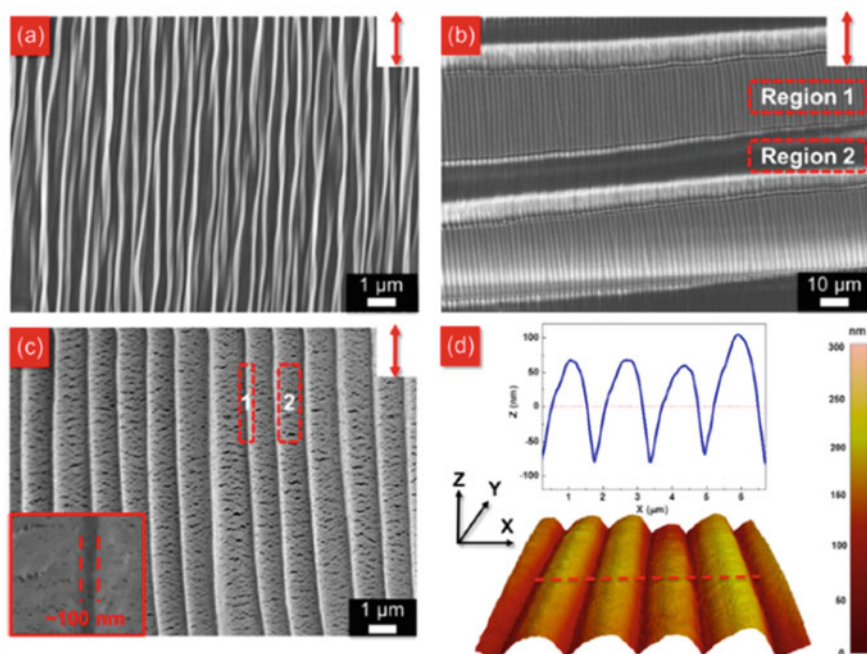


Fig. 5 Surface morphology of stretched polymer SPR film without (a) and with (b, c) 25 nm Ag film. The arrows denote the direction of externally applied stress. The polymer SPR film at a width of 4 cm is drawn from 4 cm (initial length) to 10 cm (stretched length). The inset in panel c shows the dimension of the nano-groove. The dashed boxes in panel c indicate the nano-groove (1) and nano-gaps (2), respectively. (d) Morphologies of four complete periods of polymer SPR film demonstrate 3D wave-shaped structures. The inset in panel d illustrates line scanning obtained across the dashed line. Adapted with permission from Xu et al. (2017), copyright (2020) American Chemical Society

thus forms the Ag ribbons with nano-grooves. The nano-gaps are formed during the drawing process since the deposited Ag layer is not single crystalline but consisting of many Ag particles, when subjected to large deformation, the nano-gaps formed on the boundaries between each particle. The nano-gaps function as hotspots and make the Ag/PCL film a good photonic surface for using in SERS. Compared to unstretched film, the stretched Ag/PCL film provides an enhancement (more than 10 times) in SERS, as Fig. 6 shows.

Au, Ni, and Al have been used as the deposition layer, and the surface morphology is shown in Fig. 7. For Au/PCL composites, similar surface morphology of Ag/PCL can be observed. After cold drawing, Au ribbons with wrinkles (nano-grooves and nano-gaps) are obtained. It can be used as a photonic surface for enhanced SERS as well. For Ni and Al, different surface morphology is found. The deposited metal layer fragmented into a web-like network. The different ductility and adhesion to the PCL layer lead to the distinct morphologies.

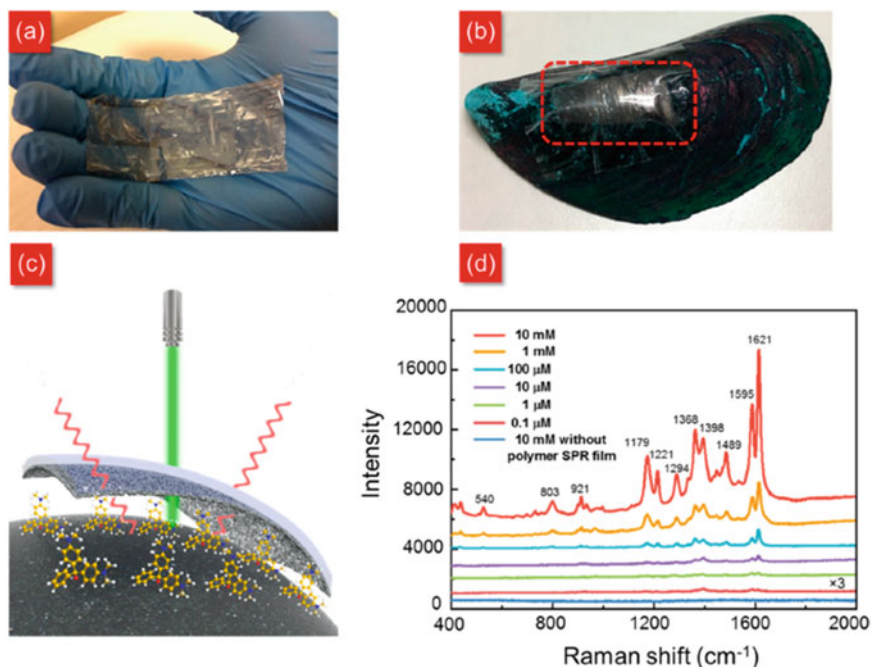


Fig. 6 Demonstration of flexible polymer SPR film for practical SERS applications. **a** A photograph image of stretched polymer SPR film (8 cm \times 4 cm). **b** A photograph image of polymer SPR film attached to the green mussel surface contaminated by MG molecules. **c** Schematic diagram of contacting polymer SPR film onto the green mussel and collecting the SERS signals from the backside surface. **d** In situ detection of MG molecules on the green mussel surface at various concentrations from 10 mM to 0.1 μ M. The SERS spectra are obtained at the laser excitation wavelength of 514 nm, where the power is 1.5 mW, the acquisition time is 10 s, and the accumulation time is 1 s. Adapted with permission from Xu et al. (2017), copyright (2020) American Chemical Society

Polycarbonate (PC) film can be used as a polymer film matrix as well. Different from semicrystalline PCL, PC is an amorphous polymer with a Poisson ratio of ~ 0.3 . A layer of Au in different thickness (Fig. 8g) was deposited onto PC (125 μ m thick) via e-beam. After the cold drawing process, the Au layer fractured into strips and no wrinkle observed. Au layer with different thicknesses from 10 to 50 nm has been studied, and similar surface morphology is found. The average width of resulted Au stripes is proportional to the thickness as shown in Fig. 8f. After cold drawing, the Au/PC composites are subjected to drawing again at the perpendicular direction (2D stretching). The Au strips are torn into distributed Au islands. The fragment length for Au layers with different thicknesses is shown in Fig. 8g.

The cold drawing of Cu and Pt layer (20 nm) deposited PC composites is studied for further investigations. After cold drawing, Cu and Pt fractured into strips similar to the Au strips. And the surface morphologies of Cu/PC and Pt/PC are islands-like, similar to the results in Au/PC (Fig. 9). The different mechanical properties

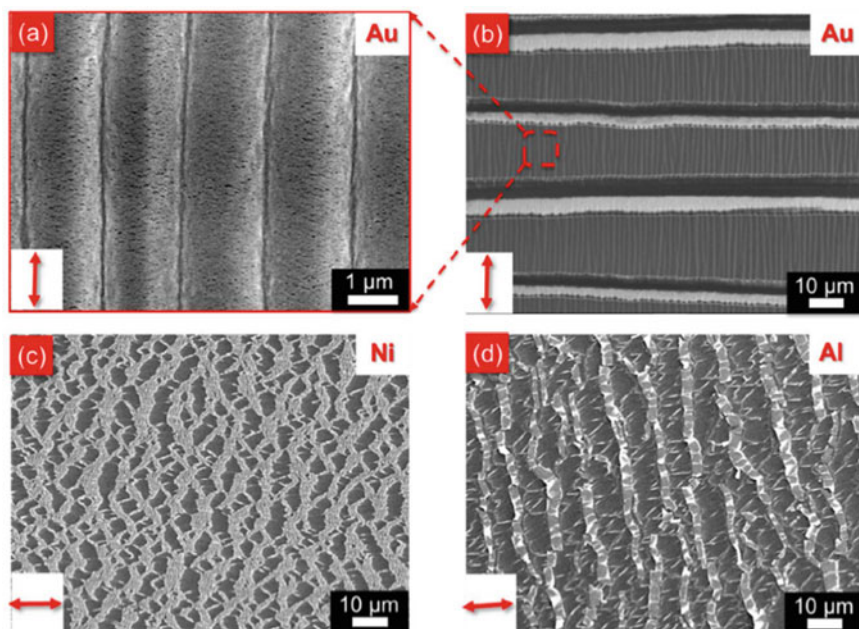


Fig. 7 Surface morphology of various metallic materials deposited on the PCL polymer films. **a**, **b** Au. **c** Ni. **d** Al. All the thicknesses of metallic films are 25 nm, and the composite film is stretched from 4 to 10 cm at a width of 4 cm. The red arrows denote the stretching direction. Adapted with permission from Xu et al. (2017), copyright (2020) American Chemical Society

and adhesion to the metal layer of PC and PCL films determine the distinct surface morphologies for metal layer after cold drawing.

The fabricated Au/PC film is highly conformal, flexible, and semitransparent, and it can be used on complex surfaces for on-site SERS sensing. As an example, the on-site SERS sensing on basil leaves and apples has been studied using the cold-drawn Au/PC film. The schematic process is shown in Fig. 10a. After cold drawing, the resulted films are attached to the surface of the leaves and apples with different concentrations of thiram. The detection of thiram residue on foods is crucial as the thiram can lead to serious health issues (Wang et al. 2015). The strongest Raman peak for thiram is at $\sim 1376\text{ cm}^{-1}$, and it is monitored during the test of on-site SERS sensing. The results are demonstrated in Fig. 10c and e. As can be seen, for the basil leaves, the lower limit of detection (LOD) for thiram using Au/PC film is about 48 ng/cm^2 , and it is 0.48 ng/cm^2 for apples. The different LOD values may arise from the surface morphologies and tissue compositions.

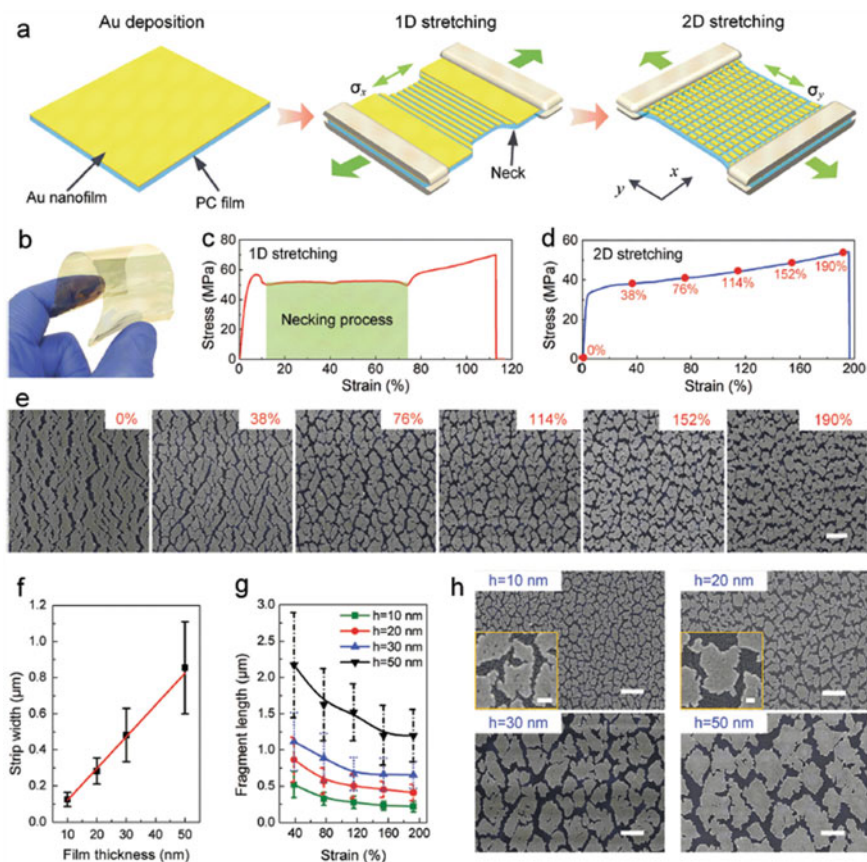


Fig. 8 Fabrication and characterization of gold nano-patterns. **a** Schematic illustration showing the fabrication process of metallic micro/nano-patterns on flexible substrates through two-step mechanical stretching. **b** Photograph of a centimeter-scale flexible photonic surface fully covered with gold nano-patterns fabricated by 2D stretching. **c, d** Stress–strain curves for the gold/PC film composite in 1D and 2D stretching processes, respectively. **e** SEM images of the gold patterns at different stages of 2D stretching (thickness of the gold film, 30 nm). **f** Average width of the gold strips fabricated by 1D stretching as a function of gold film thickness. **g** Average length of the gold patterns at different stages of 2D stretching. **h** SEM images of the 2D gold patterns with different thicknesses (strain, 152%). Scale bars: **(e)** 2 mm; **(h)** 1 mm; inset picture, 100 nm. Reproduced from Li et al. (2018) with permission from the Royal Society of Chemistry

3.2 Two-Dimensional Materials–Polymer Composites

Materials structuring using the cold drawing method have been proven to be highly effective, low cost and suitable for mass production. It is natural to think whether this method can be applied to two-dimensional materials. Different from bulk materials, two-dimensional materials have their unique properties in many aspects, and

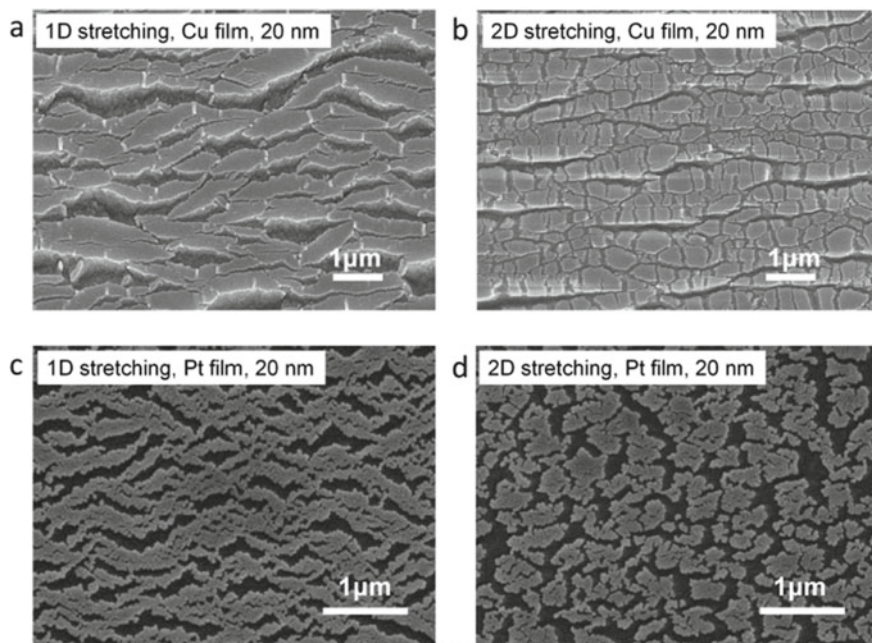


Fig. 9 SEM images of nano-patterns fabricated from copper and platinum nano-films. **a** Copper nano-strips after 1D stretching. **b** Copper nano-patterns after 2D stretching. **c** Platinum nano-strips after 1D stretching. **d** Platinum nano-patterns after 2D stretching. Film thicknesses, 20 nm; substrate, 125- μm -thick PC film; elongation for 2D stretching, 152%. Reproduced from Li et al. (2018) with permission from the Royal Society of Chemistry

their excellent electrical and mechanical properties make them a good candidate for flexible electronics (Zhang et al. 2016; Yang et al. 2017; Liu et al. 2014; Gong et al. 2016; Castellanos-Gomez et al. 2012; Bertolazzi et al. 2011). Many researches work on two-dimensional material-based flexible electronic devices are focused on two-dimensional materials/polymer assembly thanks to the superior flexibility of polymers. Thus, the investigation of cold drawing on two-dimensional materials/polymer composites not only develops a potential fabrication tool for two-dimensional ribbons but also gaining an understanding of the mechanical behaviors in two-dimensional materials/polymer assembly, which is essential for the evaluation of device stability for related flexible electronics. In the family of two-dimensional materials, the TMDs and graphene attract many interests. They are transferred onto a 125 μm PC film via the wet transfer method and then subjected to cold drawing.

Figure 11 shows the experimental process for the cold drawing of CVD-grown single crystal monolayer WS_2 on PC film. The resulted WS_2 submicron ribbons can be observed clearly using a fluorescence microscope (Fig. 11e). The ordered fragmentation of WS_2 only happens in the necking front, as Fig. 11b–d shows. Figure 11f–j gives a clearer comparative view of three WS_2 crystals before and after the cold drawing process.

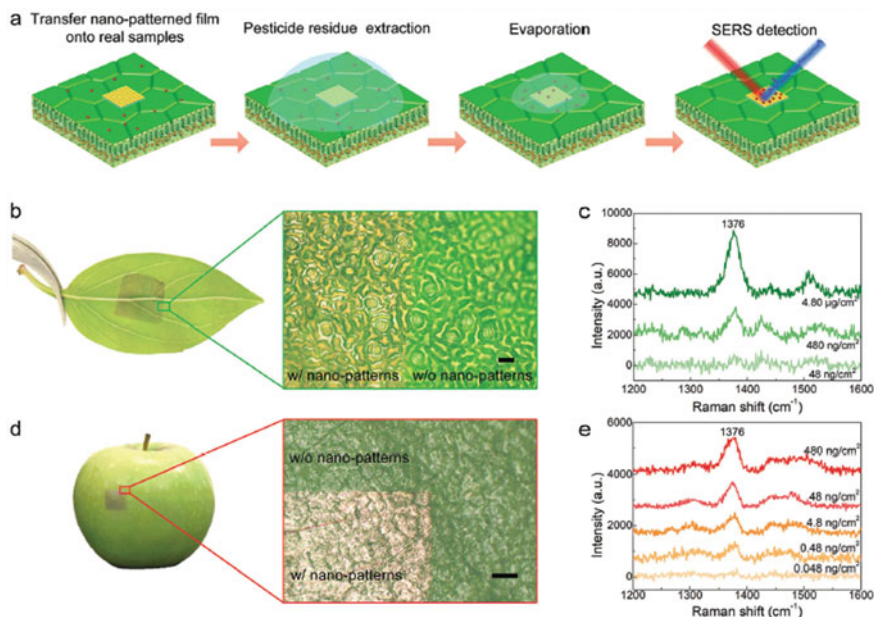


Fig. 10 Ultra-flexible and conformal gold nano-patterned film for on-site SERS sensing. **a** Schematic illustration showing the process of on-site SERS sensing. **b** Photograph of a basil leaf coated with an ultra-flexible gold nano-patterned film and micro-graph of the surface morphology. **c** On-site SERS spectra acquired using ultra-flexible gold nano-patterned films from basil leaves with different concentrations of the thiram residue (background subtracted). **d** Photograph of an apple covered with an ultra-flexible gold nano-patterned film and micro-graph of the surface morphology. **e** On-site SERS spectra acquired using ultra-flexible gold nano-patterned films from apple peels with different concentrations of the thiram residue. Scale bar: (b) 50 μm ; (d) 100 μm . Reproduced from Li et al. (2018) with permission from the Royal Society of Chemistry

The ordered fragmentation also occurs on few-layer WS_2 after the cold drawing, as shown in Fig. 12d, e. To study the versatility of this method, monolayer MoS_2 , MoSe_2 , and WSe_2 are also investigated under different drawing speeds. Again, the drawing speed is proven to have neglectable effects on the fragmentations. And similar to WS_2 , other TMDs also fractured into ordered ribbons array. The resulted ribbons have many freshly produced edges and have a better performance on hydrogen evolution reaction (HER). Figure 13 shows the comparison of HER performance over MoS_2 ribbons array-based and pristine WS_2 -based bottom-gated field-effect transistors (FETs). The MoS_2 ribbons array-based FET has enhanced performance on HER.

As another representative two-dimensional material, graphene is the thinnest and strongest material ever found. Also, large-scale polycrystalline graphene can be grown using CVD. The results for cold drawing of graphene/PC film are shown in Fig. 14.

After cold drawing, the graphene sheet was torn into submicron ribbons array. This versatile method can be applied to small single crystals and large-scale polycrystals.

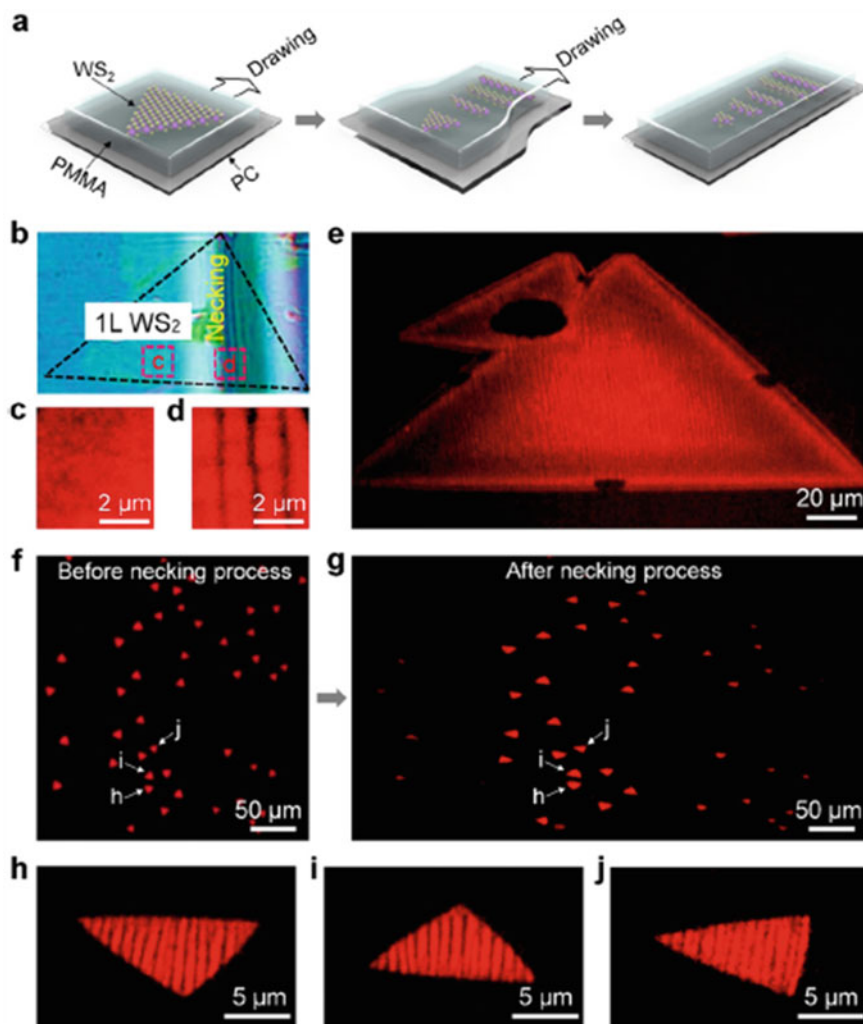


Fig. 11 Fragmentation of monolayer WS₂ via mechanical instabilities. **a** Schematic of the experimental steps to fragment monolayer WS₂. **b** Optical image of a monolayer WS₂ during the necking process, highlighting the propagating mechanical instabilities, wherein fragmentation occurs. The triangle represents 1L WS₂. **c, d** Fluorescence images of monolayer WS₂ during the necking process, corresponding to the dashed rectangles c and d in (b). **(d)** After necking propagation, WS₂ monolayers are fragmented into well-ordered nano-ribbons. **(c)** Before necking process, WS₂ monolayers are maintaining integrity. **e** Fluorescence image of a monolayer WS₂ with sample size of ~100 μm after necking process. **f** Fluorescence images of WS₂ monolayers before (located on SiO₂/Si surface) and **g** after necking process (drawing speed: 0.1 mm/s). **h–j** Magnified fluorescence images of monolayer WS₂ nano-ribbons with different orientations, corresponding to (h), (i) and (j) in (f) and (g). Adapted with permission from Chen et al. (2017), copyright (2020) American Chemical Society

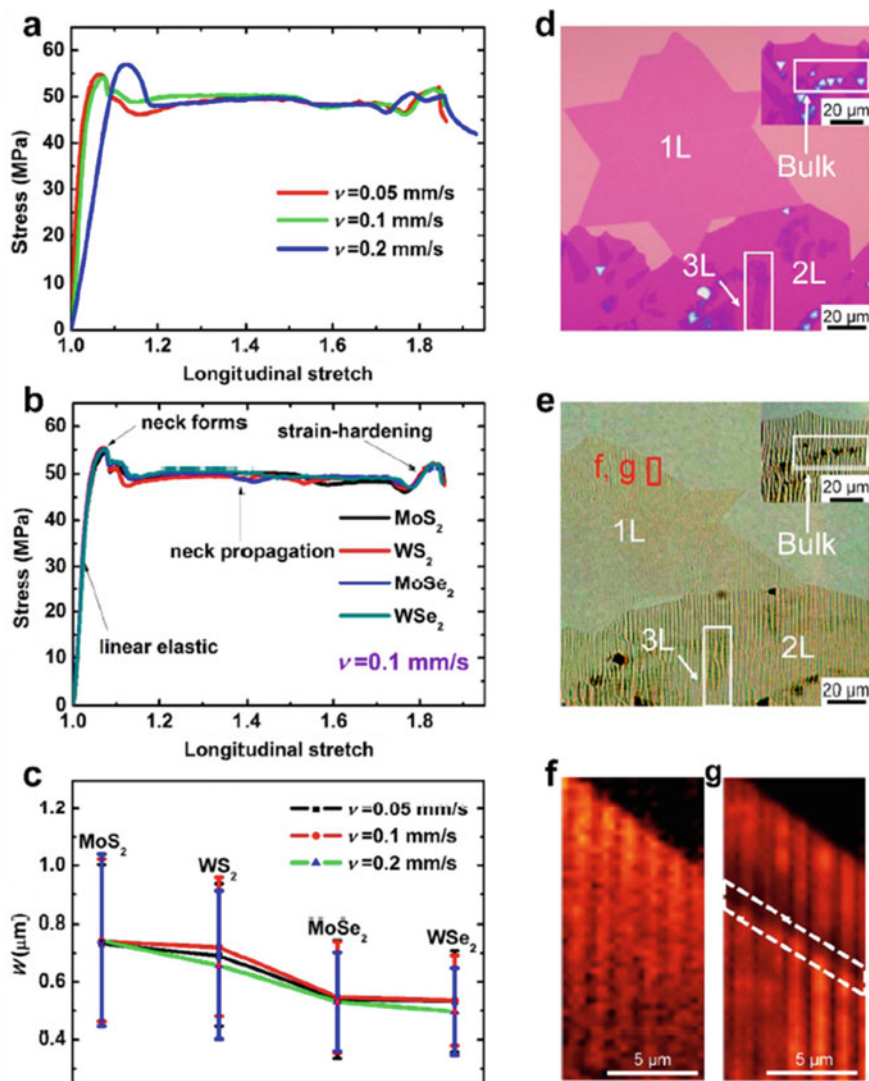


Fig. 12 Fragmentation of atomically thin TMDs via mechanical instabilities. **a** Stress–strain measurements of PC/WS₂ monolayers/PMMA at different drawing speeds. **b** Stress–strain measurements of PC/TMDs monolayers/PMMA at drawing speed of 0.1 mm/s. **c** Width of fragmented TMDs monolayers at different drawing speeds. **d**, **e** Optical images of mono- to multilayer thick WSe₂ film before and after the necking process, respectively. **f**, **g** Raman and PL mapping images (mapping at the $A_1' + E'$ mode and the strongest PL peak from the A exciton) of the section in (**e**) enclosed in a red solid rectangle. The dashed white parallelogram in (**g**) shows the grain boundary in the monolayer WSe₂. Adapted with permission from Chen et al. (2017), copyright (2020) American Chemical Society

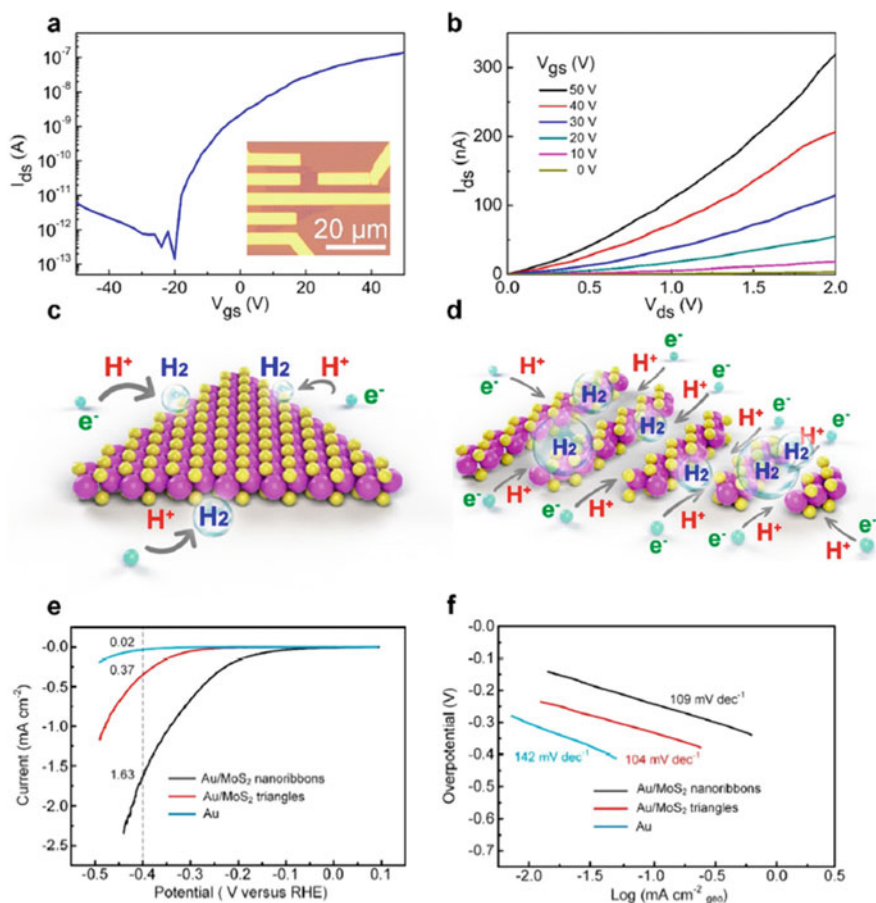


Fig. 13 Electrical properties of the fabricated monolayer MoS₂ nano-ribbons and its electrochemical performance for hydrogen evolution reaction (HER). **a** Transfer characteristic ($I_{ds} - V_{gs}$) of the FET at $V_{ds} = 1$ V, showing an on/off ratio of 106. Inset shows the fabricated FET device based on MoS₂ nano-ribbon arrays. The Si/SiO₂ substrate with the SiO₂ thickness of 270 nm is used as bake-gate. Source/drain (S/D) metal contacts are defined by electron beam lithography, and Cr/Au (5/50 nm) is deposited by thermal evaporation followed by the lift-off process. The channel width $W \sim 10 \mu\text{m}$ and channel length $L \sim 2 \mu\text{m}$. **b** Output characteristics ($I_{ds} - V_{ds}$) of the FET under different gate voltages ranging from 0 to 50 V. **c, d** Schematic representations illustrate the function of the edges of the monolayer MoS₂ triangle and monolayer MoS₂ nano-ribbons as the active sites for HER. **e, f** HER polarizing curves and Tafel plots for supporting Au (cyan), monolayer MoS₂ triangles (red), and monolayer MoS₂ nano-ribbons (black). Adapted with permission from Chen et al. (2017), copyright (2020) American Chemical Society

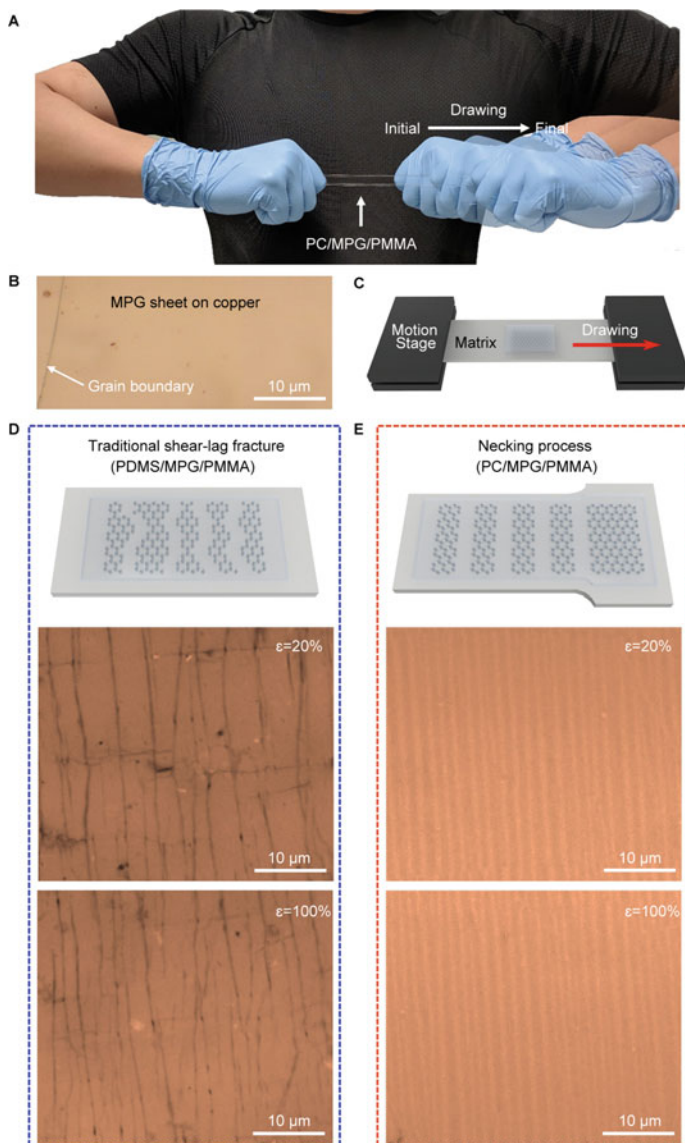


Fig. 14 Fragmentation of Monolayer Polycrystalline Graphene Sheet on a Polydimethylsiloxane Substrate versus on a Polycarbonate Substrate. **a** Photograph of a PC/MPG/PMMA sample undergoing necking process under axial stress. **b** An optical image of the initial MPG sheet on copper. **c** Schematics of MPG sheet under necking processes. **d** Schematics of MPG sheet under the traditional shear-lag fracture (PDMS/MPG/PMMA) and optical morphologies of MPG sheet under the traditional shear-lag fracture with an applied strain of 20% and 100%, respectively. Cracks are random, and the sizes of the fragment pieces decrease as the strain increases. **e** Schematics of MPG sheet under the necking process (PC/MPG/PMMA) and optical morphology of MPG sheet under the necking process with an applied strain of 20% and 100%, respectively. MPG sheet is fragmented into well-ordered ribbons with similar sizes at different strains. Adapted with permission from Chen et al. (2019)

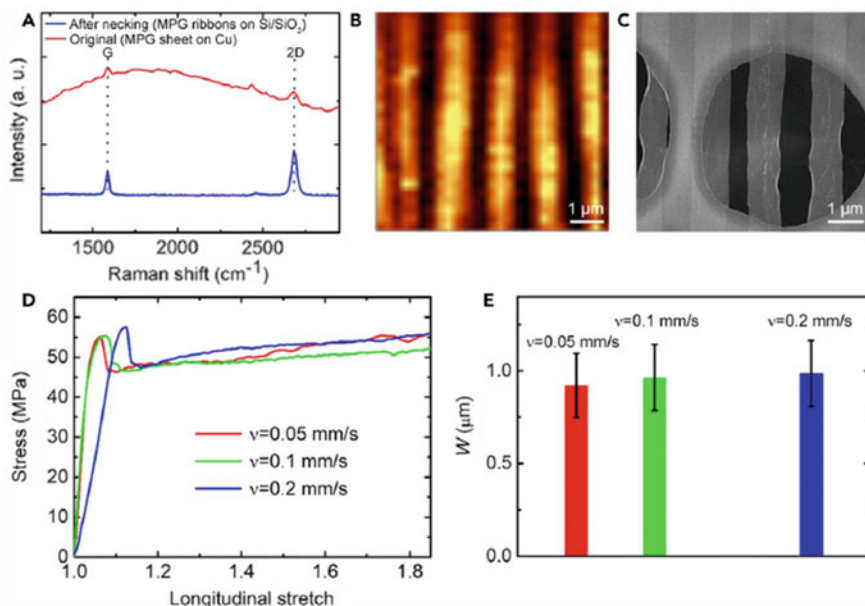


Fig. 15 Spectroscopic and Microscopic characteristics of MPG Ribbons. **a** Representative Raman spectra of MPG in different process steps. **b, c** Representative Raman mapping (**b**) and SEM (**c**) images of the resulting MPG ribbons. **d** Stress–strain measurements of PC/MPG/PMMA at different drawing speeds. **e** Width of the resulting MPG ribbons at different drawing speeds. The error bar is the SD. Adapted with permission from Chen et al. (2019)

The scale of two-dimensional materials has no limit on the occurrence of ordered fragmentation.

The Raman spectra in Fig. 15a demonstrate the high quality of resulted graphene ribbons. The morphology of graphene ribbons is further investigated using AFM and tunneling electron microscopy (TEM). The AFM and TEM images are shown in Fig. 15b, c, respectively.

To demonstrate the potential of resulted graphene ribbons on flexible electronics, the graphene sheet-based and ribbons-based FETs are fabricated and tested on nitrogen-doping and pH sensing. Compared to graphene sheet and sheet-based FETs, the graphene ribbons have an enhanced nitrogen-doping effect and the ribbons-based FET shows a higher sensitivity as the ribbons array owns a larger number of active edges, as shown in Fig. 16.

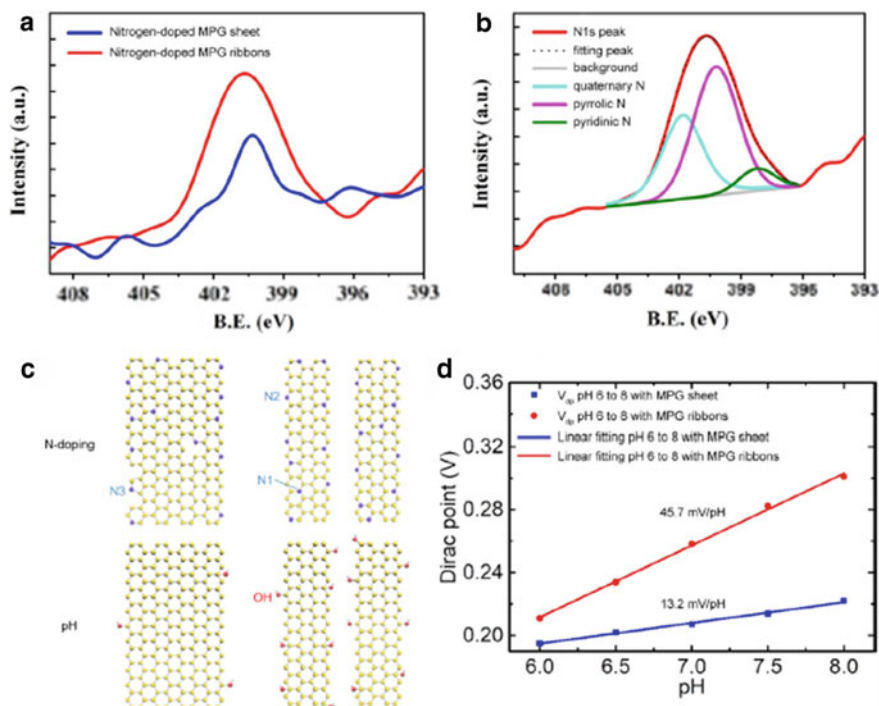


Fig. 16 Enhanced nitrogen-doping effect and pH response performance based on the fabricated MPG ribbons. **a** High-resolution XPS spectra of N1s region of nitrogen-doped MPG sheet and MPG ribbons. **b** Spectrum of N1s region of nitrogen-doped MPG ribbons showing contributions from pyrrolic, pyridinic, and quaternary nitrogen species. **c** Bonding configurations for nitrogen atom (N1, quaternary nitrogen; N2, pyridinic nitrogen; N3, pyrrolic nitrogen) and hydroxyl groups in nitrogen-doped MPG sheet and MPG ribbons. **d** V_{Dir} position versus pH for MPG sheet (blue) and MPG ribbons (red), including linear fittings to the data points (solid lines). Adapted with permission from Chen et al. (2019)

4 Conclusions

Cold drawing, a classic manufacturing process, has been rediscovered as a low-cost robust fabrication tool for materials nano- and micro-structuring. There are mainly two different geometries using in the study, core-shell structured fiber and film-based flat composites. After cold drawing, ordered fragmentation occurred. Using the core-shell fiber structures, micron rods can be produced, and micro-ribbons can be obtained by the film-base flat structures, both on a large scale. The fragmentation process can be analyzed by the shear-lag theory, which explains the mechanical behaviors on the perspective of composites and predicts the resulted morphologies of materials. This versatile method can be applied to a wide range of materials, including metals, glasses, polymers, and even two-dimensional materials. Depends on the mechanical properties of the target material, different results are obtained. For metal/polymer

film-based flat composites, a network of metal strips or islands can be produced, which finds its great potential in SERS. For core materials embedded in a polymer shell, micron rods are fabricated and can be etched out for usage. The shear-lag theory is also applicable to explain the mechanical behaviors of two-dimensional materials/polymer composites. In other words, the materials structuring using cold drawing are versatile on two-dimensional materials, which enable a new platform for the study of two-dimensional material-based flexible electronics.

References

- A.S. Argon, *The Physics of Deformation and Fracture of Polymers* (New York, Cambridge, 2013)
- S. Bertolazzi, J. Brivio, A. Kis, Stretching and breaking of ultrathin MoS₂. *ACS Nano* **5**, 9703–9709 (2011)
- W.H. Carothers, J.W. Hill, Studies of polymerization and ring formation. XV. Artificial fibers from synthetic linear condensation superpolymers. *J. Am. Chem. Soc.* **54**, 1579–1587 (1932)
- C.E. Carraher Jr., *Introduction to Polymer Chemistry* (CRC Press, 2017)
- A. Castellanos-Gomez et al., Elastic properties of freely suspended MoS₂ nanosheets. *Adv. Mater.* **24**, 772–775 (2012)
- M. Chen et al., Ordered and atomically perfect fragmentation of layered transition metal dichalcogenides via mechanical instabilities. *ACS Nano* **11**, 9191–9199 (2017). <https://doi.org/10.1021/acsnano.7b04158>
- M. Chen et al., Controlled fragmentation of single-atom-thick polycrystalline graphene. *Matter* (2019). <https://doi.org/10.1016/j.matt.2019.11.004>
- B.D. Coleman, On the cold drawing of polymers. *Comput. Math Appl.* **11**, 35–65 (1985)
- S. Fakirov, D. Bhattacharyya, R.J.T. Lin, C. Fuchs, K. Friedrich, Contribution of coalescence to microfibril formation in polymer blends during cold drawing. *J. Macromol. Sci. Part B-Phys.* **46**, 183–193 (2007). <https://doi.org/10.1080/00222340601044375>
- J.C. Figueroa, T.E. Carney, L.S. Schadler, C. Laird, Micromechanics of single filament composites. *Compos. Sci. Technol.* **42**, 77–101 (1991). [https://doi.org/10.1016/0266-3538\(91\)90013-f](https://doi.org/10.1016/0266-3538(91)90013-f)
- K. Friedrich et al., Microfibrillar reinforced composites from PET/PP blends: processing, morphology and mechanical properties. *Compos. Sci. Technol.* **65**, 107–116 (2005). <https://doi.org/10.1016/j.compscitech.2004.06.008>
- C. Galiotis, A. Paipetis, Definition and measurement of the shear-lag parameter, beta, as an index of the stress transfer efficiency in polymer composites. *J. Mater. Sci.* **33**, 1137–1143 (1998). <https://doi.org/10.1023/a:1004357121802>
- Y. Gong, V. Carozo, H. Li, M. Terrones, T.N. Jackson, High flex cycle testing of CVD monolayer WS₂ TFTs on thin flexible polyimide. *2D Mater.* **3**, 021008 (2016)
- B.W. Kim, J.A. Nairn, Observations of fiber fracture and interfacial debonding phenomena using the fragmentation test in single fiber composites. *J. Compos. Mater.* **36**, 1825–1858 (2002). <https://doi.org/10.1177/0021998302036015243>
- K. Li et al., Formation of ultra-flexible, conformal, and nano-patterned photonic surfaces via polymer cold-drawing. *J. Mater. Chem. C* **6**, 4649–4657 (2018). <https://doi.org/10.1039/c8tc00884a>
- K. Liu et al., Elastic properties of chemical-vapor-deposited monolayer MoS₂, WS₂, and their bilayer heterostructures. *Nano Lett.* **14**, 5097–5103 (2014)
- G. Loke, W. Yan, T. Khudiyev, G. Noel, Y. Fink, Recent progress and perspectives of thermally drawn multimaterial fiber electronics. *Adv. Mater.* e1904911 (2019). <https://doi.org/10.1002/adma.201904911>

- J. Loos, T. Schimanski, J. Hofman, T. Peijs, P.J. Lemstra, Morphological investigations of polypropylene single-fibre reinforced polypropylene model composites. *Polymer* **42**, 3827–3834 (2001). [https://doi.org/10.1016/s0032-3861\(00\)00660-1](https://doi.org/10.1016/s0032-3861(00)00660-1)
- J.A. Nairn, On the use of shear-lag methods for analysis of stress transfer unidirectional composites. *Mech. Mater.* **26**, 63–80 (1997). [https://doi.org/10.1016/s0167-6636\(97\)00023-9](https://doi.org/10.1016/s0167-6636(97)00023-9)
- S. Shabahang et al., Controlled fragmentation of multimaterial fibres and films via polymer cold-drawing. *Nature* **534**, 529–533 (2016). <https://doi.org/10.1038/nature17980>
- E.T. Thostenson, W.Z. Li, D.Z. Wang, Z.F. Ren, T.W. Chou, Carbon nanotube/carbon fiber hybrid multiscale composites. *J. Appl. Phys.* **91**, 6034–6037 (2002). <https://doi.org/10.1063/1.1466880>
- P. Vincent, The necking and cold-drawing of rigid plastics. *Polymer* **1**, 7–19 (1960)
- X. Wang, B. Zhang, S. Du, Y. Wu, X. Sun, Numerical simulation of the fiber fragmentation process in single-fiber composites. *Mater. Des.* **31**, 2464–2470 (2010). <https://doi.org/10.1016/j.matdes.2009.11.050>
- Q. Wang, D. Wu, Z. Chen, Ag dendritic nanostructures for rapid detection of thiram based on surface-enhanced Raman scattering. *Rsc Adv.* **5**, 70553–70557 (2015)
- T. Wu et al., Ultrawideband surface enhanced Raman scattering in hybrid graphene fragmented-gold substrates via cold-etching. *Adv. Opt. Mater.* **7** (2019). <https://doi.org/10.1002/adom.201900905>
- K. Xu et al., Uniaxially stretched flexible surface plasmon resonance film for versatile surface enhanced Raman scattering diagnostics. *ACS Appl. Mater. Interfaces.* **9**, 26341–26349 (2017). <https://doi.org/10.1021/acsami.7b06669>
- Y. Yang et al., Brittle fracture of 2D MoSe₂. *Adv. Mater.* **29**, 1604201 (2017)
- R. Zhang, V. Koutsos, R. Cheung, Elastic properties of suspended multilayer WSe₂. *Appl. Phys. Lett.* **108**, 042104 (2016)
- A. Ziabicki, *Fundamentals of Fibre Formation* (Wiley, 1976)